Size and Thickness Effects on the Ductile Fracture Toughness of a 316 L(N) Austenitic Stainless Steel in As-Received and Aged Conditions

Sihan Cheng, Jérôme Garnier, Bernard Marini, Yazid Madi, Jacques Besson

Fatigue & Fracture of Engineering Materials & Structures

WILEY

FFEMS Fatigue & Fracture of Engineering Materials & Structures

ORIGINAL ARTICLE OPEN ACCESS

Size and Thickness Effects on the Ductile Fracture Toughness of a 316 L(N) Austenitic Stainless Steel in As-Received and Aged Conditions

Sihan Cheng[1,2] | Jérôme Garnier[1] | Bernard Marini[1] | Yazid Madi[2] | Jacques Besson[2]

[1]Service de Recherches en Matériaux et procédés Avancés, Université Paris-Saclay, CEA, Gif-sur-Yvette, France | [2]Centre des Matériaux, MINES Paris-PSL, CNRS UMR, Evry, France

Correspondence: Sihan Cheng (sihan.cheng@outlook.com)

Received: 4 February 2025 | **Revised:** 28 March 2025 | **Accepted:** 16 April 2025

Funding: This work was fully funded and supported by the French Alternative Energies and Atomic Energy Commission within the project R4G.

Keywords: austenitic stainless steel | essential work | fracture toughness | size effect | thickness effect

ABSTRACT

Measuring ductile fracture toughness for materials requires the specimen size to be large enough for the tests to be valid. The presented work investigates the size related fracture behavior of as-received and aged 316 L(N) stainless steel through an experimental approach. It focuses on the effects of the thickness and size of the specimens on the evaluated toughness. Compact tension (CT) specimens (thicknesses from 4 to 50 mm) and double edge notched tensile (DENT) specimens (thicknesses from 2 to 5 mm) were used. At as-received state, CT tests lead to a nonmonotonic evolution of fracture toughness with a maximum at a critical thickness. At aged state, there is no significant thickness effect as all tests are valid. The essential work of fracture measured with DENT specimens appears to be equivalent to $J_{0.2}$ and consequently extends the nonmonotonic evolution of the fracture toughness at small thicknesses.

1 | Introduction

Fracture toughness is a fundamental material property that characterizes a material's ability to resist crack initiation and propagation when subjected to mechanical loading. The initiation and propagation of a crack are controlled by the microstructure of the material and its local loading in the vicinity of the crack tip [1, 2]. Understanding the role of each material feature on the microscopic level is complex and far from being fully solved for industrial materials. However, determining the fracture toughness is paramount in various engineering applications, particularly in the design and assessment of structural components [3, 4]. This is the reason why energy-based models were developed to describe fracture from a crack at the macroscopic level [5, 6]. However, it appeared rapidly that the macroscopic fracture toughness of a material is not an intrinsic physical property and is influenced by numerous factors, such as the thickness, size, and geometry of the specimens used to determine this property [7–10].

These facts are taken into account by standards like ASTM E1820 [11] or ISO 12135 [12]. Specimens have a precise geometry and must be large enough to ensure that the fracture toughness qualified can be considered size-independent. According to both standards, the fracture toughness test is conducted by applying an increasing displacement by a tensile machine. The "single specimen" method involves applying load–unload cycles during the test. These cycles allow to determine the elastic compliance, which is used to estimate the crack length. A curve, referred to as the $J-R$ curve, relating the J-integral to crack extension

Abbreviations: CT, compact tension; DENT, double edge notched tensile; EWF, essential work of fracture; SENB, single edge notched bending; ST, smooth specimen.

Summary

- Fracture toughness (FT) is studied using 316 L(N) specimens with different size.
- A nonmonotonic evolution of $J_{0.2}$ is observed as a function of size.
- $J_{0.2}$ reaches a maximal value for a material dependent critical thickness.
- The essential work w_e seems to give an estimate of FT at small thickness.

Δa, indicates the material's resistance to crack propagation. The fracture toughness ($J_{0.2}$) is determined by the intersection of the $J-R$ curve with a blunting line with an offset of 0.2 mm. However, the slope of the blunting line is defined as $\sigma_{YS}+\sigma_{TS}$ in ASTM E1820 and $3.75\sigma_{TS}$ in ISO 12135, where σ_{YS} is the 0.2% offset yield strength and σ_{TS} is the ultimate tensile strength. To ensure the test's validity, standards define J_{max} and Δa_{max} to qualify the validity of data (Δa, J) used in the determination of $J_{0.2}$. For ASTM E1820 [11],

$$J_{max}=\min\left(\frac{b_0\sigma_Y}{10},\frac{B_0\sigma_Y}{10}\right)\text{ and }\Delta a_{max}=0.25b_0 \quad (1)$$

But for ISO 12135 [12],

$$J_{max}=\min\left(\frac{a_0\sigma_Y}{10},\frac{b_0\sigma_Y}{10},\frac{B_0\sigma_Y}{10}\right)\text{ and }\Delta a_{max}=0.25b_0 \quad (2)$$

where a_0 is the initial crack length, b_0 is the initial remaining ligament length, B_0 is the initial specimen's thickness, and $\sigma_Y=0.5(\sigma_{YS}+\sigma_{TS})$. When the point of $J_{0.2}$ is less than J_{max} for a crack advance less than Δa_{max}, the test is considered as valid, meaning that the value of $J_{0.2}$ is independent of specimen's size and thickness.

However, miniaturized specimens are still interesting for the industrial qualification of thin structure or heterogeneous materials. The effect of specimen thickness and size on ductile fracture toughness has been the subject of extensive research for decades.

Ono et al. [13] tested a ferritic steel using CT specimens with the same size but different thickness (6.35~24 mm) according to standard ASTM E1820-99a [14]. The fracture toughness, measured by calculating the J-integral, increases as the specimen thickness decreases. Their explanation is that when the specimen's thickness decreases, the state of plane stress becomes predominant, and the size of the plastic zone at the crack tip increases. Since the energy consumed by plastic deformation increases, the fracture toughness increases. In the study by Mahmound and Lease [15], the critical value of crack tip opening angle (for stable crack propagation) is considered to be a measurement of fracture toughness. It decreases as the thickness of CT specimens of aluminum alloy 2024-T351, which varies from 2.3 to 25.4 mm.

In the study of Kang et al. [9], double-edge cracked specimens of copper foils with thicknesses ranging from 0.02 to 1 mm were tested in tensile loading until fracture occurred. A digital speckle correlation method was adopted to assess strain fields around the crack tip to determine the J-integral. A nonmonotonic evolution of fracture toughness with thickness was found. When the thickness is less than a critical thickness, the fracture toughness increases with increasing thickness. However, beyond the critical thickness, it then drops with increasing thickness. According to their fractographic study, Zhang et al. also noted a change in fracture mode from "brittle"/shear-mode fracture to a mixed shear-mode/ductile fracture when thickness increases. This change makes the work in crack-tip necking and the work in material separation increase with thickness at first and decrease after a maximum. This evolution of fracture toughness with thickness is also found in other studies [16, 17]. However, Seok and Kim's studies [18] on a SA515 steel show little effect of thickness reduction on fracture toughness according to their toughness tests on CT specimens with thickness from 12.7 to 50.8 mm.

Pardoen et al. [19, 20] conducted a series of experiments with double edge notched tensile (DENT) specimens of 6082T0 aluminum to study the influence of thickness using the "essential work of fracture" method [21–24]. The fracture toughness of DENT specimens can be characterized by the essential work (w_e) and J-integral at crack initiation (J_c). In the studies by Pardoen et al. [19, 20], when the DENT specimen's thickness increased from 1 to 6 mm, both w_e and J_c exhibited a linear increase in the case of thinner specimens, while for thicker specimens, the relationship between J_c and thickness is nonlinear decreasing. In addition, w_e and J_c have equivalent values for small thicknesses. The method based on the "essential work of fracture" has been studied for many different materials such as metal sheets [23–25], high-strength aluminum alloys [26], and polymers [27, 28]. These studies indicate that the ligament length must be well chosen. In the study by Cotterell et al. [23], the minimum ligament length should be 3–5 times the specimen's thickness to maintain a plane stress configuration. The maximal ligament length is determined to avoid the spread of plastic to the border of specimen [21]. This generally requires the ligament to be one-third of the specimen's width.

Many studies show that fracture toughness, measured with CT, single-edge notched bending (SENB) or Charpy specimens, decreases when reducing the specimen's size [13, 29]. This is not always the case. For example, Wardle [30] examined tests on side-grooved CT specimens of A533C1.1 steel from 10 to 100-mm thick conducted at room temperature and 288°C. He found no significant effect of specimen size on fracture toughness. Tests on SENB specimens with thicknesses between 5 and 20 mm also led to the same conclusion.

The above review shows that the effects of thickness and size on fracture toughness are not fully understood. Toughness appears to be a function of material and specimen geometry. The present study investigates the effect of specimen thickness and size on the ductile fracture toughness of a 316 L(N) stainless steel. Two very different material conditions are investigated: as-received (high toughness) and aged for 2000 h at 750°C (low toughness). First, metallographic observations are made to observe the microstructure. Tensile tests are performed to characterize the elastoplastic behavior. Thickness and size effects are studied

by fracture toughness tests using CT and DENT specimens of different sizes. Elastoplastic finite element simulations are performed on the different geometries of the fracture specimens to verify the consistency of the database.

2 | Materials and Methods

2.1 | Materials

The austenitic stainless steel 316 L(N) is widely used in the nuclear domain for its high ductility and toughness, as well as its good weldability and corrosion resistance [31, 32]. It is a candidate material for the fourth generation of nuclear reactors. The material is delivered in the form of a cylinder with a diameter of 2000 mm and height of 350 mm, which was forged by Aubert & Duval. It is a very low-carbon (0.023 wt%) and nitrogen-controlled (0.07 wt%) austenitic alloy. The material is used in the as-received condition and a severely aged condition. The aging treatment is performed in an oven at 750°C for 2000 h. This treatment reduces the mechanical properties by promoting the creation of intra and intergranular carbides [33, 34]. In the following, the as-received state is marked as M1, and the aged state is marked as M2. The microstructure of the material in two states is studied by electron back-scattered diffraction (EBSD) analysis in a scanning electron microscope (SEM). There is no remarkable difference in grain size after aging at 750°C[35]. The mean grain size (without twins) is 154 μm at the as-received state (M1) and 169 μm at the aged state (M2). Twins are found in both states.

At the as-received state (M1), there are some spherical inclusions at grain boundaries and in grains, as shown in Figure 1a. Its chemical composition is analyzed by X-ray mapping in a SEM. It is found that inclusions have an Al-O base and a core/shell structure with a Ca-S enriched shell and a Ca-Mg enriched core [35, 36]. At the aged state (M2), many intergranular and intragranular precipitates [37, 38] of micronic and submicronic size are present, as shown in Figure 1b. The X-ray mapping results in Figure 1b show that there are two types of precipitates. Intergranular precipitates are rich in chromium and molybdenum, consistent with the sigma phase [33, 39, 40]. Intragranular precipitates are mainly enriched in molybdenum and correspond to the Laves phase [33, 39, 41]. M23C6 carbides could also be present mainly at grain boundaries.

Tensile tests were carried out on smooth specimens (ST) at room temperature to characterize the material's behavior. ST specimens have a diameter of 6 mm and a gage length of 34 mm. They were taken in different sampling orientations in order to verify the isotropy of the material. The transverse strain was also measured using an edge tracing method [42–45]. A digital camera and LED lamps were installed on two sides of the specimen. Then, the specimen's shadow can be recorded by camera. All recorded images were analyzed thanks to a Python script [45, 46], which can detect the specimen's contour and then measure the minimum diameter (ϕ) of the specimen. For all tensile tests, the displacement rate was equal to $2.5\ 10^{-4}\ s^{-1}$. Time, load, actuator displacement, and extensometer opening were recorded during the test.

The ST test results for both states show good isotropy of the 316 L(N) stainless steel. Figure 2 shows an example of a nominal stress versus nominal strain ($F/S_0 - \Delta l/l_0$) and nominal stress versus diameter reduction ($F/S_0 - \Delta\phi/\phi_0$) for ST tests. A large work hardening ($\sigma_{TS} > 2\sigma_{YS}$) is observed for both states [47]. However, the strain at failure at the aged state (M2) is about 50% of the value at the as-received state. The maximal stress is larger in the aged state than in the as-received state. As expected, the aging treatment greatly reduced the ductility but reinforced the strength of the 316 L(N) steel [48, 49]. The reduction of area is measured according to the following equation:

$$Z = \frac{S_0 - S_f}{S_0} \tag{3}$$

where S_0 is the initial cross-section and S_f the cross-section at failure. After aging, the necking coefficient is reduced significantly up to 2 times (78% vs. 39% as measured on the fracture surface).

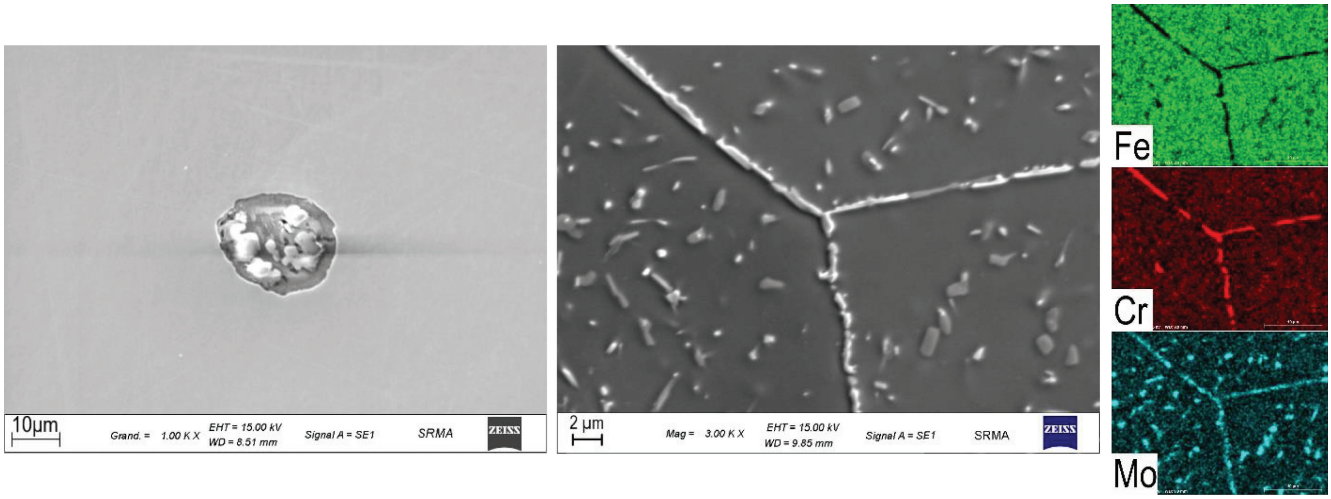

(a) Inclusions at as-received state (M1) (b) Precipitates at the aged state (M2)

FIGURE 1 | Metallographic photos in SEM. [Colour figure can be viewed at wileyonlinelibrary.com]

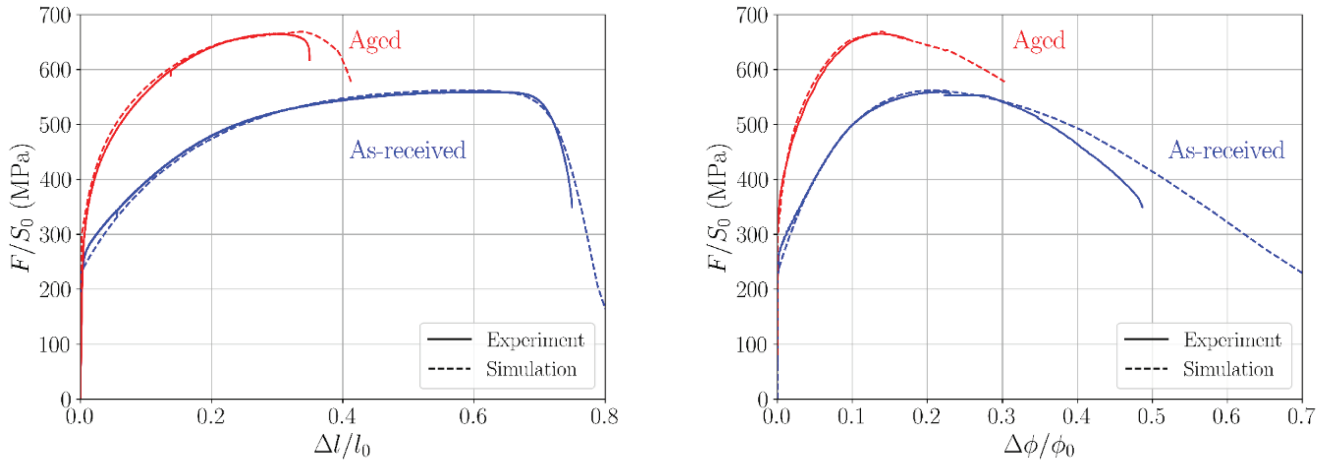

(a) $F/S_0 - \Delta l/l_0$ (b) $F/S_0 - \Delta\phi/\phi_0$

FIGURE 2 | Experimental and numerical tensile curves of ST specimens. [Colour figure can be viewed at wileyonlinelibrary.com]

TABLE 1 | Results of identification of plastic law.

State	R_0 (MPa)	Q_1 (MPa)	b_1	Q_2 (MPa)	b_2
As-received (M1)	231.5	1463.8	0.736	260.7	5.325
Aged (M2)	300.0	715.5	3.955	107.2	59.614

TABLE 2 | Geometries of CT specimens.

	As-received state (M1)								Aged state (M2)						
W (mm)	25						50	100	8	25				50	100
B_0 (mm)	5	7.5	10	12.5	20	25	25	50	4	5	7.5	10	12.5	25	50
B_0/W	0.2	0.3	0.4	0.5	0.8	1	0.5	0.5	0.5	0.2	0.3	0.4	0.5	0.5	0.5

Tensile test results provide the database for identification of the elastoplastic behavior of 316 L(N) stainless steel. 2D axisymmetric meshes of tensile specimens are shown in the Appendix. The plastic flow of 316 L(N) is described by a von Mises criterion with an evolution of the flow stress R described by a double Voce model [43, 45, 50] as follows:

$$R(p) = R_0 + Q_1\left(1 - \exp\left(-b_1 p\right)\right) + Q_2\left(1 - \exp\left(-b_2 p\right)\right) \quad (4)$$

where p is the accumulated equivalent plastic strain and R_0, Q_1, b_1, Q_2, b_2 are parameters to be adjusted. This model can describe the multistage hardening behavior and improve accuracy at large strains. The values of five parameters are determined by the minimization of the objective function defined by the difference between experimental and finite element results. Only experimental data before necking is considered for each specimen. Table 1 shows the plastic law parameters identified by the optimization method. Figure 2 compares the results of simulations with experimental data. They show good agreement before the damage-controlled phase (force decreasing). As no damage model is used in simulations, the load decrease has only a geometrical cause (necking). The elongation ($\Delta l/l_0$) is well described, showing that the load drop in Figure 2a is mainly caused by plasticity. The variation in diameter Figure 2b) is overestimated as the model does not account for damage. In the following, all experiments will be simulated to check their consistency in the purely elastoplastic regime and estimate when crack extension becomes significant.

2.2 | Fracture Toughness Tests

For fracture toughness tests, CT specimens were used, which were machined according to the CT geometry in ASTM E1820. The name of CT specimen is given by CT x B y, where x is the value of the distance between the load line and the back edge of specimen (W: specimen width) and y is the value of initial thickness (B_0). In ASTM E1820, B_0 is defined as $0.5W$ and allowed to vary from $0.25W$ to $0.5W$. Then, the first series of homothetic CT specimens were machined with $B_0 = 0.5W$ and W varying from 8 to 100 mm to study the size effect. The second series of CT specimens were machined: W here was conserved as 25 mm, but B_0 varied from 5 to 25 mm to study the thickness effect. Table 2 shows a summary of CT specimens' geometries. For each geometry, three or four tests were carried out.

According to the test procedure in ASTM E1820, a crack should be introduced in CT specimens by fatigue precracking. For that purpose, CT specimens were firstly machined with side grooves having a net thickness as $B_n = 0.9B_0$, that is, a notch of 5% of the thickness B_0, which is allowed during precracking in ASTM E1820. This step was carried out on an INSTRON traction machine. The fatigue propagation was performed under a decreasing ΔK with a load ratio of 0.1 and a frequency of 10 Hz. The aimed length of this initial crack after fatigue was $a_0 = 0.6W$, which meets the criteria in the standards ($0.45W \leq a_0 \leq 0.7W$ for ASTM E1820). After precracking, final side notches were machined up to $B_n = 0.8B_0$ as proposed by ASTM E1820. Then, the fracture toughness tests were performed according to the unloading elastic compliance method. An extensometer is placed on the CT specimens to measure the crack mouth opening displacement (CMOD). The test is controlled with the CMOD measured by the extensometer with a 0.25 mm/min displacement rate. The unloading was set up at 30% of the current load. During unloading, the compliance was calculated, and the crack length was estimated according to the formulas in the ASTM E1820. During tests, the extensometer measurement and the machine load were recorded. After tests, specimens were put in a furnace at 360°C for 3 h in order to reveal by oxidation the crack surface obtained during the test. Then, they were installed again on the tensile machine to obtain the final fracture by fatigue without significant plastic strain.

2.3 | EWF Tests

The method of essential work of fracture is aimed at separating the total work of fracture (w_f) into an essential (w_e) part and nonessential part (w_p) by varying DENT specimens' thickness (t_0) and ligament length (l_0). Figure 3a shows the schematic representation of the DENT specimens. Their dimensions are

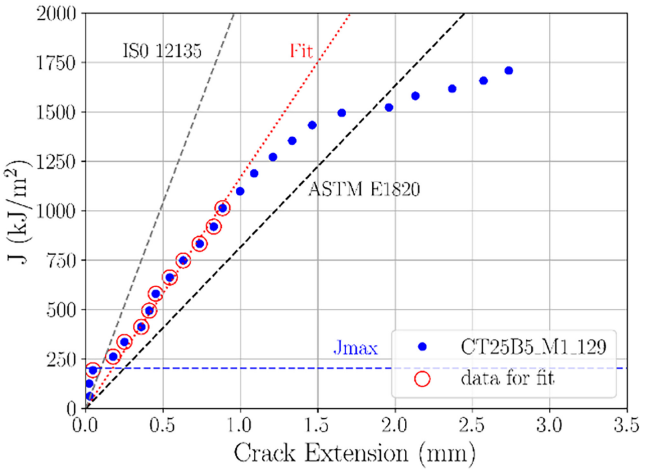

FIGURE 4 | Example of $J-R$ curves at as-received state (M1). [Colour figure can be viewed at wileyonlinelibrary.com]

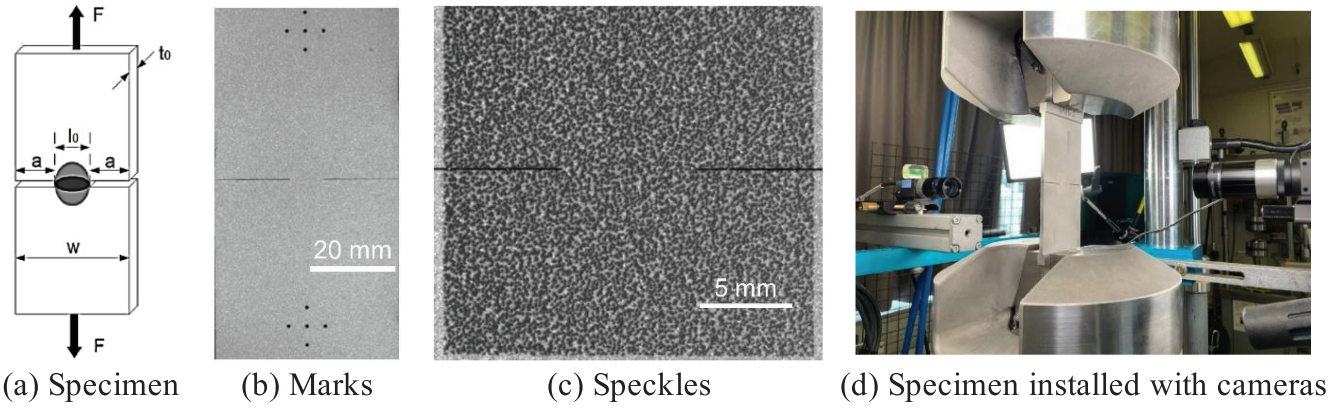

FIGURE 3 | Test conditions for EWF method with DENT specimens. [Colour figure can be viewed at wileyonlinelibrary.com]

TABLE 3 | Geometries of DENT specimens.

As-received state (M1)					Aged state (M2)				
Thickness t_0 (mm)	**Ligament l_0 (mm)**	**Height (mm)**	**Width (mm)**	**Notch radius (mm)**	**Thickness t_0 (mm)**	**Ligament l_0 (mm)**	**Height (mm)**	**Width (mm)**	**Notch radius (mm)**
2	4, 6, 8, 12, 14	150	50	0.075	2	6, 8, 12, 14	150	50	0.075
3	6, 9, 12, 15				3	6, 9, 12, 15		70	
4	12, 14, 16, 18		70		4	12, 14, 16, 18			
5	12, 14, 16, 18				5	12, 14, 16, 18			

shown in Table 3. They are determined by finite element simulations using the plastic law described above Table 1. These simulations were used to check that the plastic zone did not reach the outer edges of the specimens. Due to the geometric limitations of the grips of the MTS tensile machine, a width of 50 mm for the head of each specimen was imposed. The thickness of the specimen's head was set to 10 mm (larger than the thickness of the central part of the specimens) to fit the machine's grips. This modification does not influence the loading of specimens, which was verified through finite element simulations. All DENT specimens are noted as DENT_Ep t_0 _Li l_0, where t_0 is the thickness and l_0 is the ligament length. During the tests, the large size of the DENT specimens made setting up a physical extensometer difficult. Therefore, a virtual extensometer was employed. To do so, some point markers were made by laser on one side of the specimens, as shown in Figure 3b. The positions of the markers were chosen far enough from the plastically deformed area at a distance of 40 mm from the ligament to avoid the influence of plastic strain. The markers at the top and bottom work as multiple virtual extensometers, and the average value is taken as the elongation of the specimen. On the other side, laser speckles (Figure 3c) were created to measure the displacement fields. The surface of speckles was $25 \times 25\,\text{mm}^2$. A digital camera was set up on each side to follow simultaneously the displacements of the markers and the speckles.

Before each test, a rigid body movement up to 5 mm was performed by fixing only the lower grip in order to calibrate the displacements. Images from two cameras were processed using VIC-2D and Ariane (software developed by Centre des Matériaux). This calibration establishes the relationship between displacement in pixels and in millimeters for both cameras. They are about 0.012 mm/pixel for the camera following the speckles and 0.045 mm/pixel for the camera tracking the markers. After calibration, DENT specimens were loaded in the tensile machine (as Figure 3d) with a displacement rate of 0.2 mm/min. Photographs were recorded every 2 s in the as-received state (M1) and every 1 s in the aged state (M2). Recordings were synchronized with the force-displacement recording by digital signals. Data such as machine displacement, load, and time were recorded automatically during all the tests.

For a DENT specimen loaded in tension, the total work of fracture (W_f) can be expressed by Equation (5) [23].

$$W_f = l_0 t_0 w_e + l_0^2 t_0 w_p \quad \Rightarrow \quad w_f = w_e + l_0 w_p \tag{5}$$

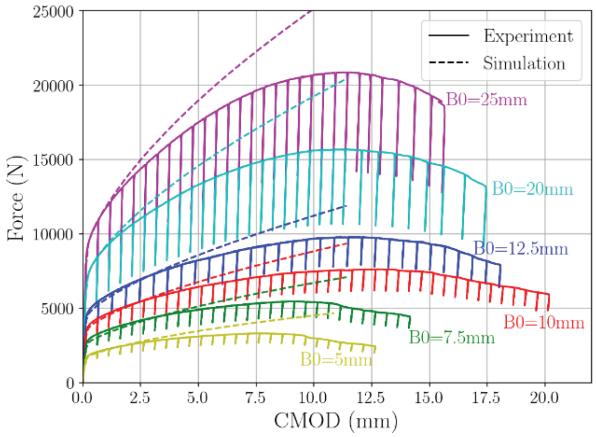

(a) Force-CMOD curves of CT25Bx at as-received state (M1)

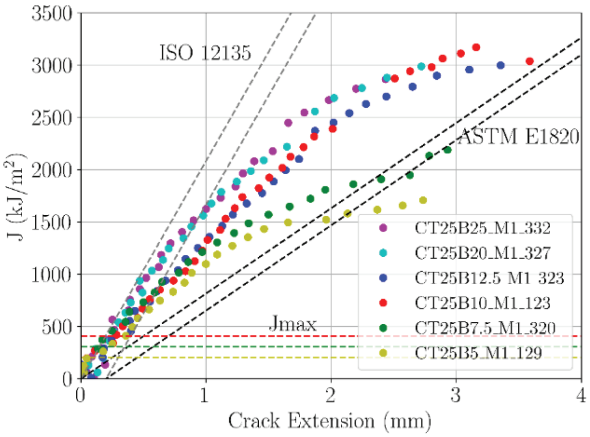

(b) $J-R$ curves of CT25Bx at as-received state (M1)

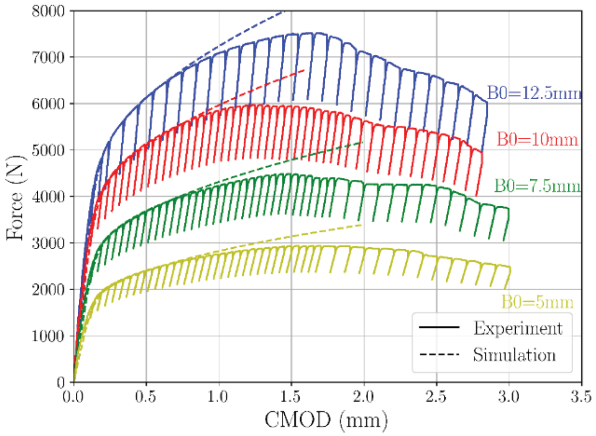

(c) Force-CMOD curves of CT25Bx at aged state (M2)

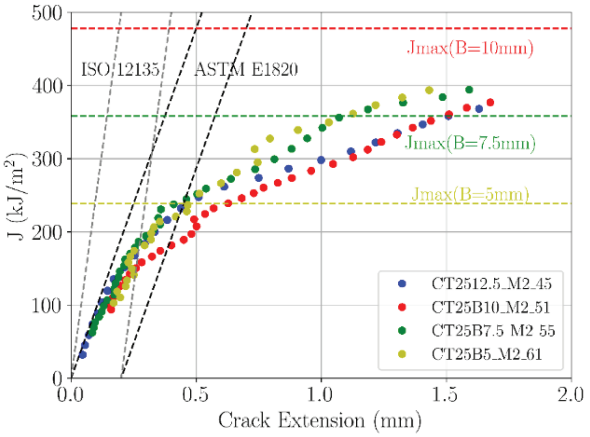

(d) $J-R$ curves of CT25Bx at aged state (M2)

FIGURE 5 | Tests results for CT25Bx specimens:force-CMOD curves and $J-R$ curves. [Colour figure can be viewed at wileyonlinelibrary.com]

Then, w_e can be obtained by conducting a linear regression on the values of w_f measured for a range of DENT specimens with different ligament lengths (l_0). On the other hand, the mean value of J-integral along the crack front of DENT specimens at crack initiation can be calculated according to Equation (6) [51].

$$J_c = \frac{K_{\mathrm{DENT}}^2}{E} + \frac{l_0}{t_0}\left(2\int_0^{\text{crack initiation}} F\mathrm{d}u_p - Fu_p\right) \tag{6}$$

where F is the load and u_p is the plastic displacement. The stress intensity factor K_{DENT} can be calculated as [52].

$$K_{\mathrm{DENT}} = \frac{F\sqrt{\pi a_0/w}}{t_0\sqrt{0.5w}\sqrt{1-a_0/0.5w}}\left[k_0 + k_1\left(\frac{a_0}{0.5w}\right) + k_2\left(\frac{a_0}{0.5w}\right)^2 + k_3\left(\frac{a_0}{0.5w}\right)^3 + k_4\left(\frac{a_0}{0.5w}\right)^4\right] \tag{7}$$

where $k_0 = 1.122$, $k_1 = -0.561$, $k_2 = -0.205$, $k_3 = 0.471$, and $k_4 = 0.19$.

3 | Fracture Toughness Results

All fracture tests were conducted following the ASTM E1820 standard using partial unloading to evaluate the specimen compliance from which the crack extension can be determined. An example of a resulting $J-R$ curve is provided in Figure 4 for a CT25B5 specimen. The blunting lines given by the ASTM E1820 and ISO 12135 are also plotted together with the value for $J_{\max}$. It is shown that J values are well above $J_{\max}$ which indicates that tests do not meet the validity criteria of the standards. It also appears that the blunting lines defined by the standards are not able to properly reproduce the initial linear part of the $J-R$ curve. Therefore, an experimental blunting line is constructed using a linear regression fitted with circled points (between 10% and 50% of the final value of J), marked by "Fit" in Figure 4. It is located between the blunting lines of the two standards. In the following, the value of $J_{0.2}$ is determined using this experimental blunting line for all the results of CT specimens.

Figure 5a shows the force-displacement curves for CT25Bx at as-received state (M1). They are compared with simulated curves using elastoplasticity. The meshes of CT specimens are presented in the Appendix. At the beginning of loading, there is a good agreement between experiments and simulation up to a CMOD of 2.5 mm. Above this value, a difference between experimental and numerical curves is observed before the maximal force. An explanation is that damage is significant before maximal force. A dependence of CMOD at maximal force ($\mathrm{CMOD}_{F\max}$) on thickness is found. $\mathrm{CMOD}_{F\max}$ increases from $B_0 = 5$ to $B_0 = 10$ mm but decrease from $B_0 = 10$ to $B_0 = 25$ mm. $J-R$ curves for CT25Bx at the as-received state (M1) are shown in Figure 5b. The slope of the experimental blunting line increases as the specimen becomes thicker. For all tests at as-received state, $J-R$ curves are out of the validity domain defined by $J_{\max}$. The values of $J_{0.2}$ (intersection of $J-R$ curve with the experimental 0.2 mm offset line) are shown in Figure 6a (red symbols) as a function of the net

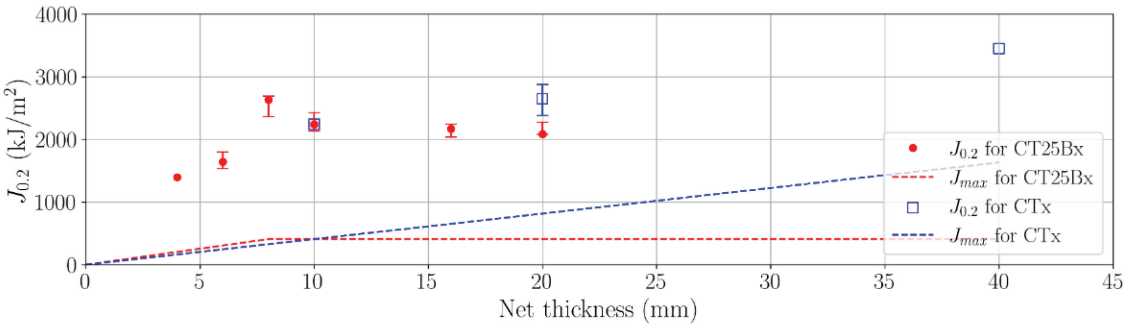

(a) Relation between $J_{0.2}$ and net thickness for CT25Bx at as-received state (M1)

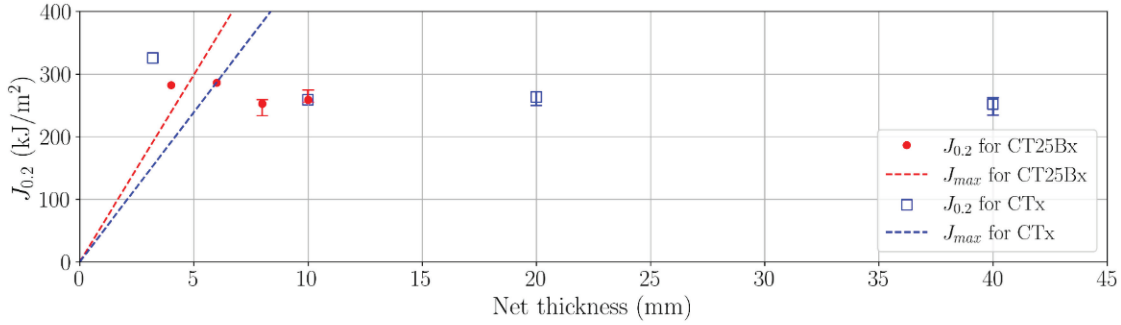

(b) Relation between $J_{0\,2}$ and net thickness for CT25Bx at aged state (M2)

FIGURE 6 | Evolution of $J_{0.2}$ as a function of thickness for CT tests. [Colour figure can be viewed at wileyonlinelibrary.com]

thickness. A nonmonotonic evolution is observed. First, an increase is observed. The maximum value for $J_{0.2}$ is reached for a net thickness of 8 mm. Above this value, a slight decrease is observed.

The same analysis is applied to tests conducted on the aged material. The results are shown in Figure 5c,d. The difference in $\mathrm{CMOD}_{F\max}$ is much smaller than for the as-received state. All four $J-R$ curves are valid. Moreover, the slopes of the blunting lines are quasi-identical and closer to the value given by ASTM E1820. During actual crack propagation, there is only a small difference when varying the specimen's thickness. Fracture toughness ($J_{0.2}$) is almost constant with thickness (Figure 6b). Therefore, it is verified that valid tests give a fracture toughness independent of the specimen thickness.

Results for homothetic CT specimens are shown in Figure 7. Figure 7a,b shows the force-CMOD curves for both materials. For the as-received state in Figure 7c, $J-R$ curves have the same blunting line. Before crack initiation (divergence from the initial blunting line), all curves are similar. However, it is observed that actual ductile tearing starts at higher J values when the specimen becomes larger [29, 53]. In all cases, $J_{0.2}$ is larger than $J_{\max}$, so that tests cannot be considered as valid based on the standards. In the aged state in Figure 7d, only the smallest specimen (CT8B4) is not valid. It shows the same blunting line as the other tests at the beginning of $J-R$ curve. But its blunting phase is longer, which leads to a higher J at crack initiation. For the other three valid tests, $J-R$ curves are almost the same even for the largest specimen with $W = 100$ mm. In all cases, the blunting corresponds to the one defined by the ASTM E1820 standard.

4 | Results on DENT Specimens and EWF

Digital image correlation allows us to visualize the strain field in DENT specimens. Figure 8 shows examples of the strain field at maximal force for both states. The maximal force is indicated by black points in force-displacement curves, as shown in Figure 9. A strain concentration is found at the notch tip, which contains the fracture process zone. Plasticity is well limited in a quasi-circular zone, especially at the as-received state (M1). When comparing both states, it clearly appears that the plastic zone is smaller at the aged state (M2) as well as the notch opening. To check for crack initiation, several tests were interrupted to make paste impressions of the notch tip. The impressions solidified at

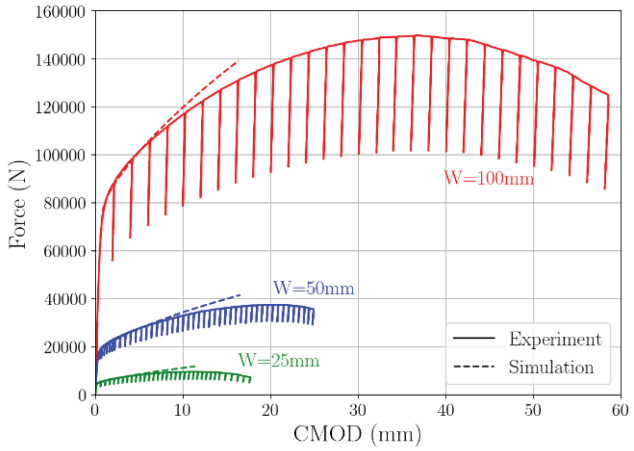

(a) Force-CMOD curves of CTx at as-received state (M1)

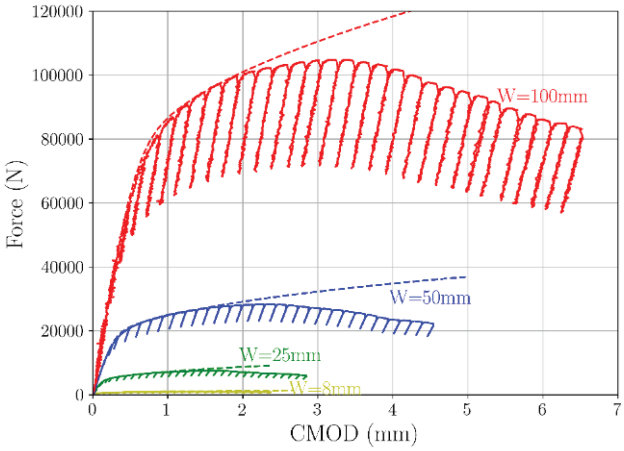

(b) Force-CMOD curves of CTx at aged state (M2)

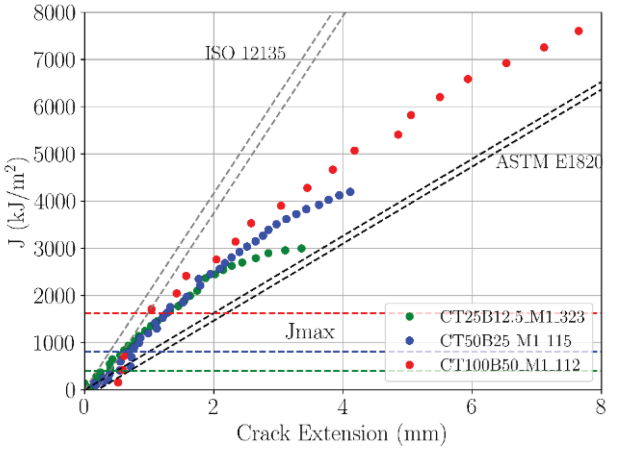

(c) $J-R$ curves of CTx at as-received state (M1)

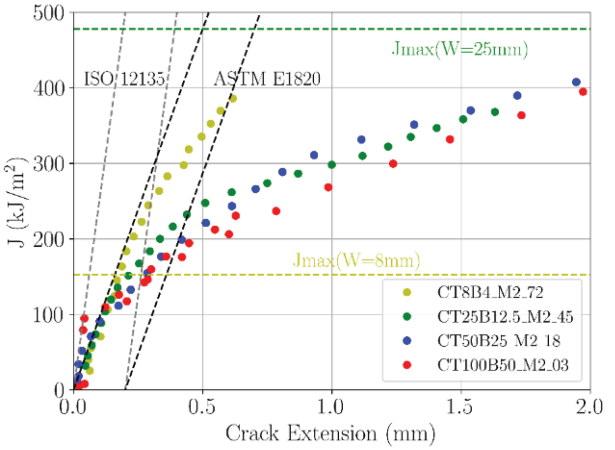

(d) $J-R$ curves of CTx at aged state (M2)

FIGURE 7 | Tests results for homothetic CT specimens: force-CMOD curves and $J-R$ curves. [Colour figure can be viewed at wileyonlinelibrary.com]

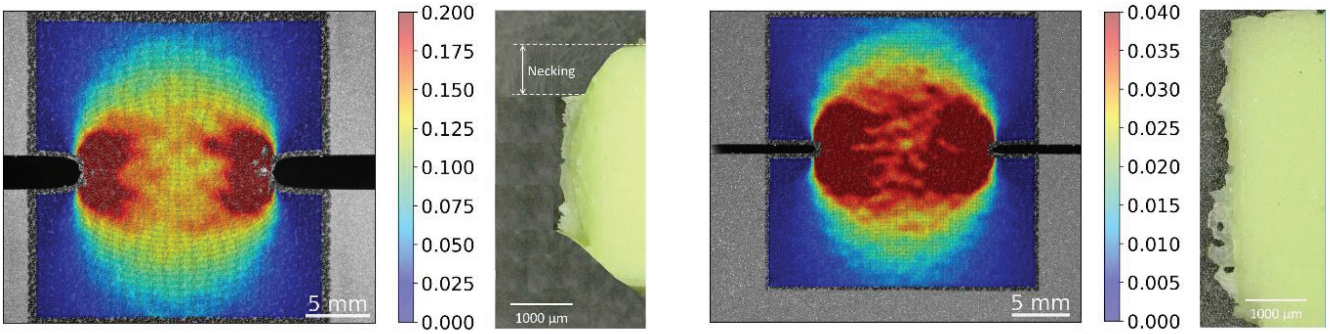

(a) DENT_Ep4_Li14 at as-received state (M1) (b) DENT_Ep5_Li14 at aged state (M2)

FIGURE 8 | Image correlation and paste impression at maximal force for DENT specimens at maximum load. [Colour figure can be viewed at wileyonlinelibrary.com]

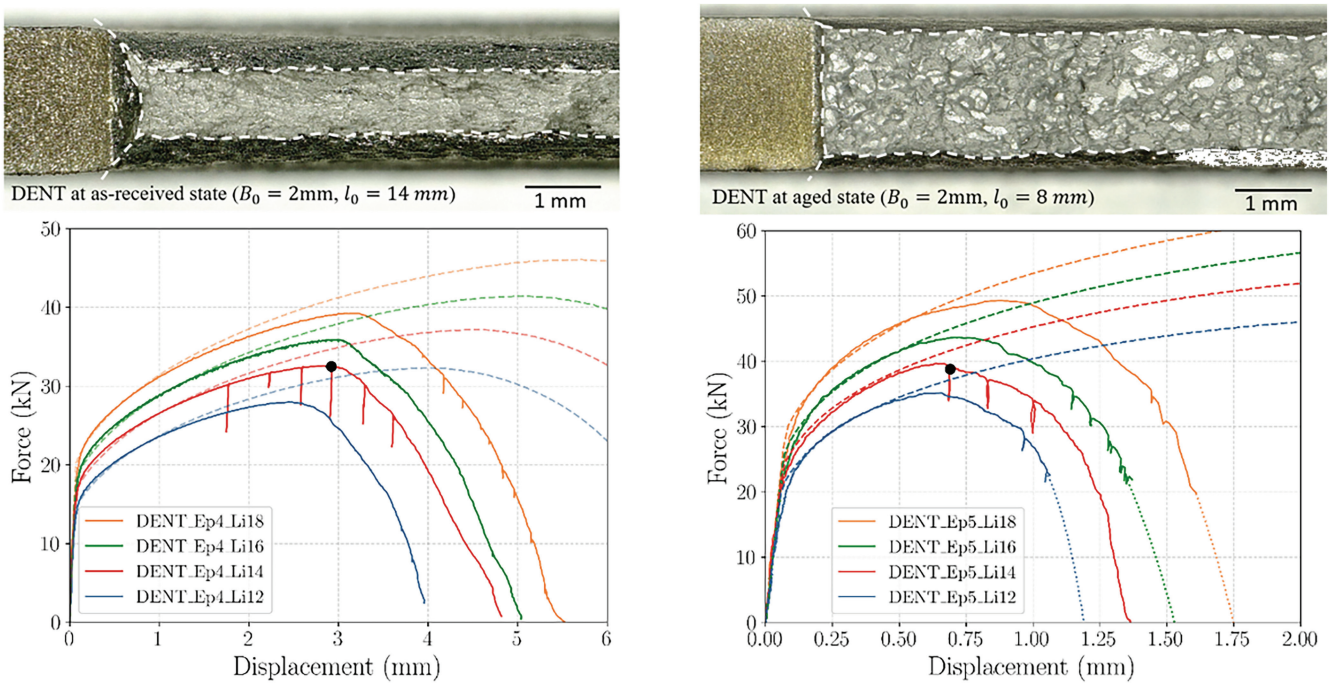

(a) As-received state (M1) (b) Aged state (M2)

FIGURE 9 | Example of force-displacement curves for DENT with a thickness of 5 mm: experimental curves in solid lines and simulation curves in dashed line. [Colour figure can be viewed at wileyonlinelibrary.com]

maximal load (black points in Figure 9) are shown in Figure 8 for both specimens. A very slight crack advance is observed for both states. It was also checked that the cracks did not initiate for a load equal to 90% of the maximum load. Therefore, it could be concluded that crack initiation happens at a load very close to the maximal force.

Examples of force-displacement curves are plotted in Figure 9a for the as-received state (M1) and Figure 10b for the aged state (M2) and compared with the corresponding FE simulations. A good match is obtained almost up to the maximum force, thus confirming that crack initiation occurs just before reaching the maximum force. A similar shape is found for all curves [21, 54]. At the as-received state (M1), there is a gradual decrease of force, which indicates a stable crack advance up to the full failure of the specimens. The work of fracture (W_f) can then be directly evaluated. In the aged state, unstable fracture occurs while the load is strongly decreasing due to the instability of the system [55]. In that case, the load–displacement curve was extrapolated (second order polynomial) to estimate W_f. The extrapolations are shown by dotted lines. This "reconstructed" curve was then used to evaluate W_f. The values of w_f for a given specimen thickness are plotted against the ligament length in Figure 10a for as-received state (M1) and in Figure 10c for aged state (M2). For each thickness, it is verified that he relation between w_f and ligament length l_0 is quasilinear. w_e is then obtained by fitting Equation (5) for each series of experiments (a series consists of samples having the same thickness but different ligament lengths). The regression slope (w_p) corresponds to the dissipated plastic energy per unit volume. It can be observed that

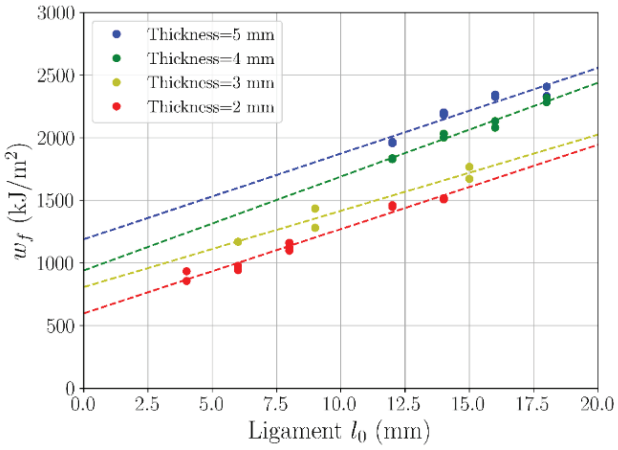

(a) Relation between total specific work of fracture (w_f) and ligament length (l_0) for DENT specimens at as-received state

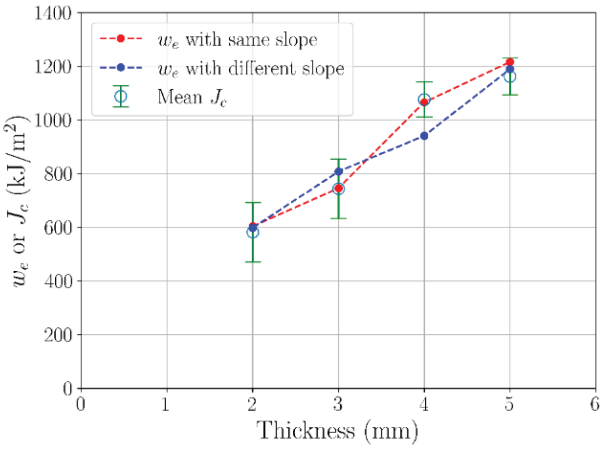

(b) Relation between specific essential work of fracture (w_e) and thickness (t_0) for DENT specimens at as-received state

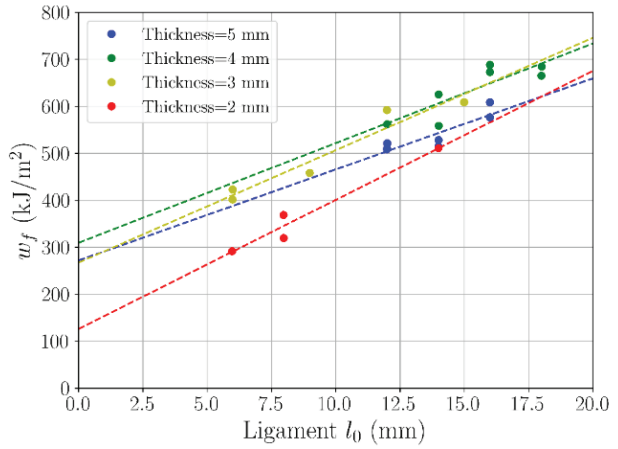

(c) Relation between total specific work of fracture (w_f) and ligament length (l_0) for DENT specimens at aged state

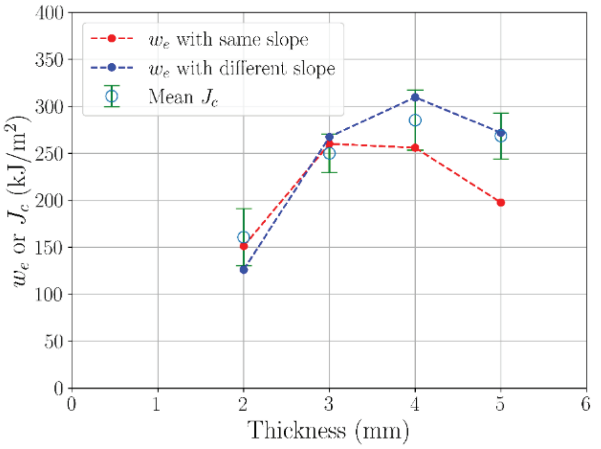

(d) Relation between specific essential work of fracture (w_e) and thickness (t_0) for DENT specimens at aged state

FIGURE 10 | Determination of essential work w_e and its evolution as a function of thickness. [Colour figure can be viewed at wileyonlinelibrary.com]

w_p is almost the same for all series. The fit was, therefore, also performed using all series and assuming a common value for w_p (referred to as $\overline{w}_p$). The resulting values for w_e are plotted against thickness in Figure 10b for the as-received state (M1) and in Figure 11d for the aged state (M2). For both fitting methods (different slopes and same slope), w_e increases linearly with thickness at the as-received state (M1). This linearity can be explained by the separation of w_e into an intrinsic part w_e^0, which is linked to damage and material separation, and another part which is due to localized necking, which is proportional to $t_0 w_e^n$, in which w_e^n represents the work dissipated at the front of crack tip [56]. Therefore, the linear increase of fracture toughness (w_e) is due to the contribution of localized necking. However, the evolution of w_e with thickness is not monotonic at the aged state (M2). There is an increase from $t_0 = 2$ to 4 mm and a decrease for $t_0 = 5$ mm. This is because the contribution of necking to the fracture energy is small for the M2 material. In addition, the J-integral is also calculated using Equation (6) to get the critical value J_c for each specimen. Then, an averaged value of J_c together with the scatter band is plotted in green. They are plotted in Figure 10b,d. An equivalence is found between w_e and the average value of J_c. In particular, they both have the same evolution with thickness [10, 28, 57]. Globally, there is no significant difference between w_e from linear regression with different slopes and the same slope. But at the aged state, the linear regression with the same slope gives a lower value of w_e at thicknesses of 4 and 5 mm (Figure 10d). These two values of w_e also show less coherence with J_c.

5 | Fractographic Examinations

Fractographies of tensile tests are shown in Figure 11. At the as-received state (M1), the cross-section is strongly reduced but keeps a quasicircular shape, showing that deformation is isotropic (Figure 11a). At position d in Figure 11a, large dimples can be found in the center zone with a diameter of about 150 μm (Figure 11d). Between large dimples, the fracture

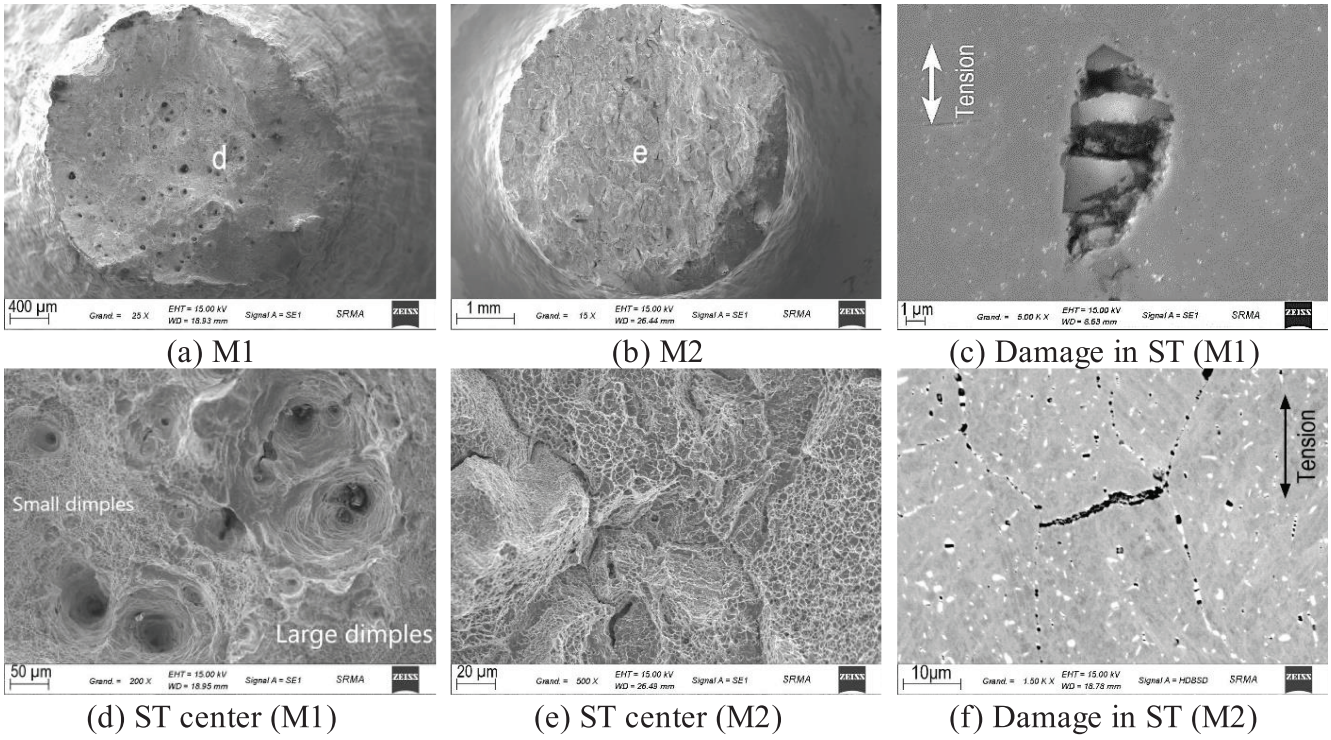

FIGURE 11 | Photographs of fracture surfaces and damage on polished cross-sections for tensile specimens (SEM observation). (a) Macroscopic view (M1 material). (b) Macroscopic view (M2 material). (c) Polished cross-section showing damage in material M1. (d) Fractographic view at the center of a specimen (M1). (e) Fractographic view at the center of a specimen (M2). (f) Polished cross-section showing damage in material M2. [Colour figure can be viewed at wileyonlinelibrary.com]

surface is covered with much smaller dimples. Some cases of coalescence by internal necking [58, 59] are observed between dimples grown from close inclusions. In the outer zone, there are fewer large dimples (Figure 11a). After tests, the broken ST specimens were axially sectioned and polished to perform SEM observations of damage below the fracture surface. An example of damage at the as-received state is shown in Figure 11c. It is an inclusion which is multifractured perpendicular to the tensile direction. This type of damage is at the origin of the large dimple mentioned above. In the aged state, the deformation at fracture is smaller, and the fracture surface is more planar, as shown in Figure 11b. There are no large dimples but only small ones [2]. The grain boundaries are easy to identify on the fracture surface, and secondary cracks can be observed [48, 60], as shown in Figure 11e. Figure 11f shows damage on the polished cross-sections. Damage is mainly located on precipitates. The largest observed damage is a crack along a grain boundary perpendicular to the tensile direction. Damage at grain boundary parallel to tensile direction consists of cavities nucleated on precipitates. Moreover, intragranular precipitation appears to lead to less damage [61, 62].

For the as-received state, four different zones can be identified on the fracture surface of CT specimens: the fatigue precrack, the blunting zone, the crack propagation, and the final fatigue crack. The blunting zone begins at the limit of precrack and ends at the first dimple and is formed at the beginning of the test before the crack initiation [63]. Its width is about 1 mm which is characteristic of the high toughness of this material. On the propagation fracture surface, inclusions are observed in large dimples (Figure 12a). At the aged state, the blunting zone is almost inexistant, which is consistent with the low value for $J_{0.2}$. Large dimples are not found in the propagation zone (Figure 12c). The macroscopic fracture surface reveals polyhedral volumes looking like grains. There are also several secondary cracks perpendicular to the fracture surface probably formed by grain boundary cracking. Small dimples are observed all over the fracture surface. Coarse inclusions are found but the cavities which contain them show very little growth compared to what was observed on the as-received material.

Figure 9 compares the macroscopic fracture surfaces of two DENT specimens. As expected, the thickness reduction as well as blunting are much larger for the as-received condition. SEM observations show no evidence of significant differences between CT and DENT specimens. In the as-received condition, large dimples are observed in the center of the specimens (Figure 12b), and smaller dimples are observed near the free surface and near the initial notch where blunting occurs. Grain boundary ductile failure with small dimples is observed in the aged condition (Figure 12d). There is also no significant difference when comparing specimens of different thicknesses. Therefore, the size and density of dimples do not appear to be dependent on the specimen thickness and, therefore, on stress triaxiality.

An EDS analysis of fracture surfaces for the aged condition was carried out. Results are shown in Figure 13, where it is possible to identify two zones. Zone (a) contains very small dimples, whereas Zone (b) has a rougher aspect. Zone (a) has a higher

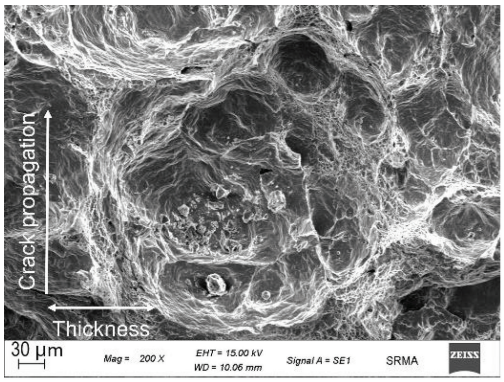

(a) Large dimples in the propagation zone of CT specimen at the as-received state (M1)

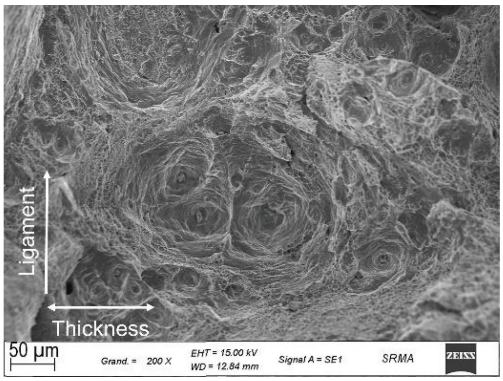

(b) Large dimples on the fracture surface of DENT specimens at the as-received state (M1)

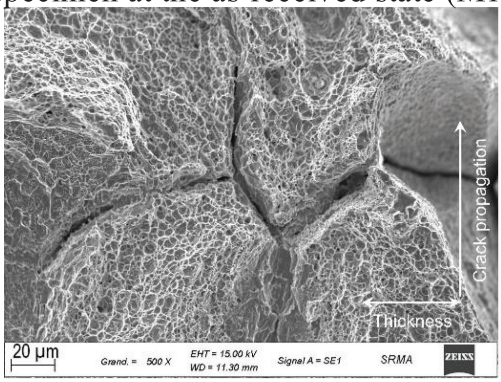

(c) Mini-dimples and grain separation in propagation zone of a CT specimen at the aged state (M2)

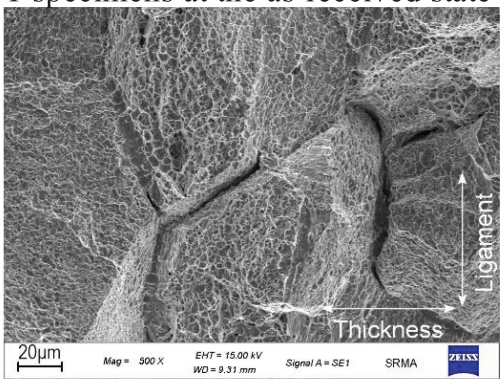

(d) Mini-dimples and grain separation on the fracture surface of DENT specimens at the aged state (M2)

FIGURE 12 | Photographs of fracture surface for CT specimens (SEM observation). [Colour figure can be viewed at wileyonlinelibrary.com]

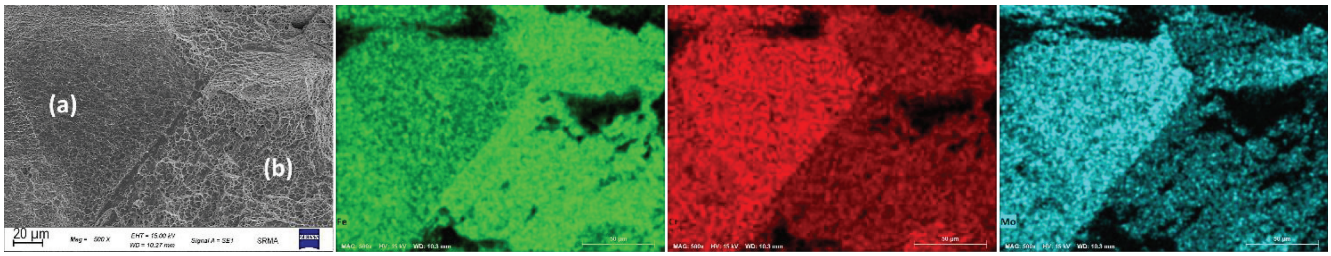

(a) SEM observation (b) Fe (c) Cr (d) Mo

FIGURE 13 | Chemical composition of fracture surface by EDS. [Colour figure can be viewed at wileyonlinelibrary.com]

chromium and molybdenum content. Based on the observations of polished cross-sections in Figure 1b, Zone (a) corresponds to intergranular fracture and Zone (b) to intragranular fracture. Both types of surfaces have roughly the same occurrence rate. This mixed fracture mode is consistent with the results of Wang et al. [62]. The same fracture mode was observed in all specimens.

6 | Discussion

In this study, fracture toughness tests on as-received and aged 316 L(N) steels were conducted using CT specimens and analyzed using either ASTM E1820 or ISO 12135 standards. In terms of validity conditions, both standards are close. ISO 12135 introduces an additional validity condition (see Equation (2)), where a_0 is also used to define J_{max}. However, this condition was never considered in this study as $b_0 < a_0$ for all test cases. The main difference between both standards is the definition of the slope of the construction line, which is always larger in the case of the ISO 12135 standard ($\sigma_{YS} + \sigma_{TS}$ (ASTM) vs. $3.75\sigma_{TS}$ (ISO)). This leads to a systematically smaller value for $J_{0.2}$ using the ISO 12135 standard. In the case of the as-received material, neither formula worked. The experimental slope was always greater than the ASTM slope and always smaller than the ISO slope. To solve this problem,

the slope was fitted to the experimental data and then used to determine $J_{0.2}$. This procedure was proposed in ASTM E1820-08a [64] but was removed in the following versions [11, 65], probably because a risk of nonconservative determination of $J_{0.2}$. Using this procedure, all CT tests on the as-received material were considered as invalid, but a value for $J_{0.2}$ could be determined. Conversely, a very good agreement was found between the ASTM formula and the experimental results. For that reason, values using the ASTM standard were preferred. For fracture toughness, all tests on the aged material could be considered valid except for the very small CT8B4 specimen.

Figure 14 compares $J_{0.2}$ determined on CT specimens and w_e measured on DENT specimens. It is worth remembering that w_e is very close of the value of $J_{0.2}$ determined using Equation (6) (see Figure 10b,d). Values of w'_e, corresponding to the value fitted of w_e fitted using a single slope for all test series (w_p independent on the thickness), are also indicated. At the as-received state, the evolution of w_e allows extending the evolution of $J_{0.2}$ at low thickness. For a thickness close to 5 mm, w_e (DENT) and $J_{0.2}$ (CT) have similar values. Considering CT25 specimens with different thicknesses (CT25Bx), the maximum value of the toughness is reached for a critical thickness (B_c) equal to 8 mm and is equal to 2633 kJ/m^2. Below B_c, toughness strongly increases. Above B_c, a small decrease is observed ($J_{0.2}$ reaches about 2085 kJ/m^2) up to a thickness of 25 mm. The strongly decrease often reported in the literature [9, 16] is not observed. Considering other geometries for CT specimens (CT50B25 and CT100B50), a constant value of $J_{0.2}$ is not observed; the highest value is obtained for the largest specimen (3450 kJ/m^2 for the CT100B50 specimen which, despite its size, is not valid). This significant variation in fracture toughness can clearly be attributed to the fact the tests are not valid according to the standards. At the aged state, w_e is also observed to sharply increase up to a thickness of 4 mm which corresponds to the critical value B_c for this material state. For this critical thickness, values of w_e (SENT) and $J_{0.2}$ (CT)

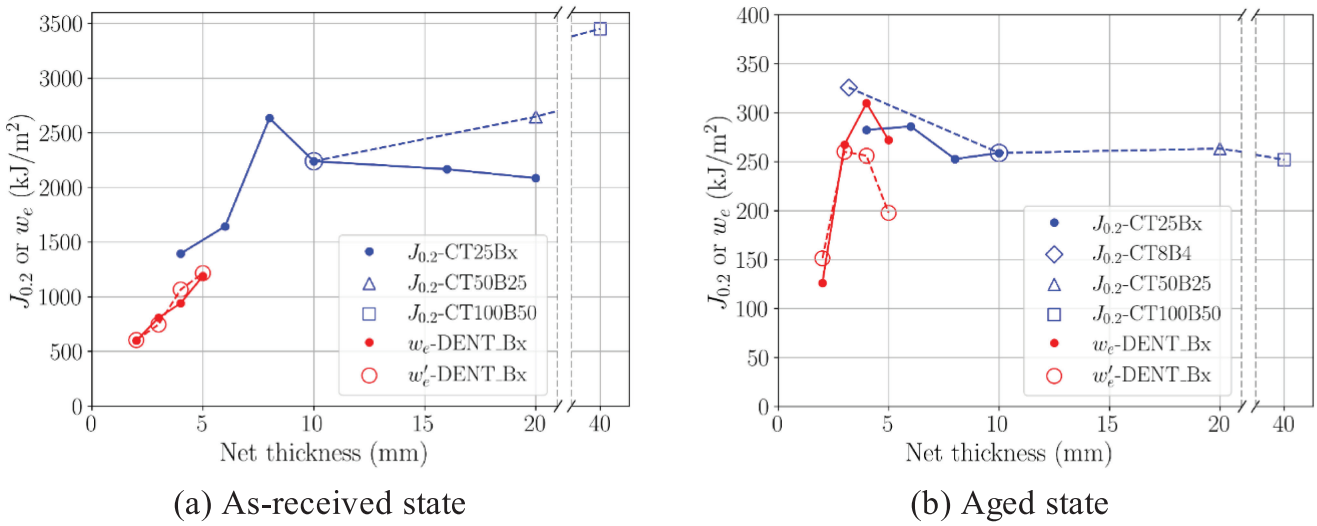

FIGURE 14 | Relation between fracture toughness ($J_{0.2}$ and w_e) and net thickness. [Colour figure can be viewed at wileyonlinelibrary.com]

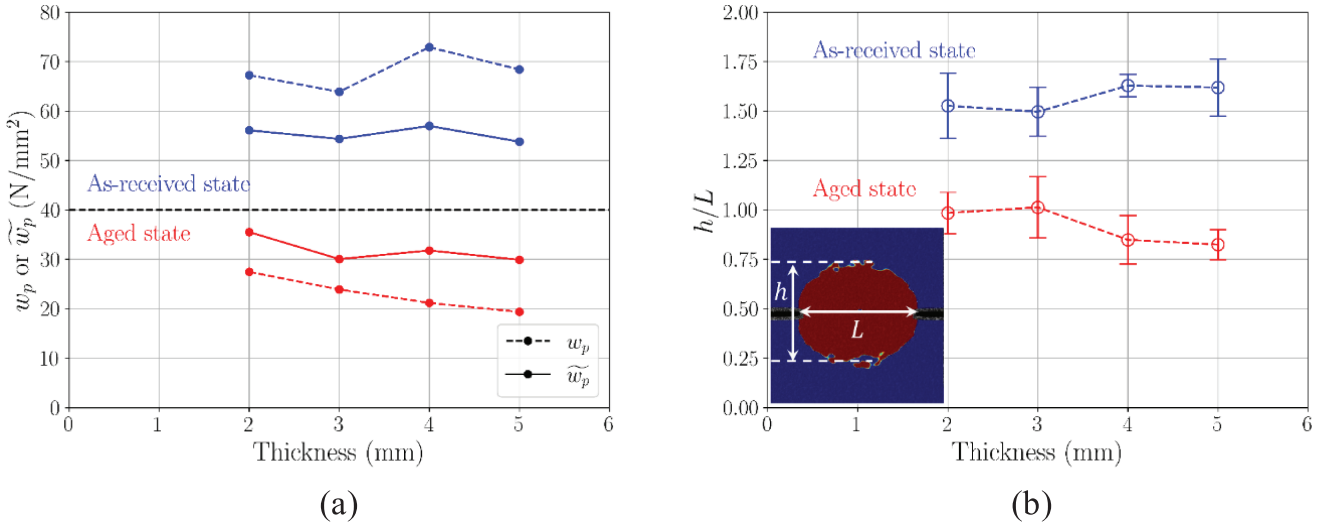

FIGURE 15 | Evolution of w_p and $\tilde{w}_p$ (a) and h/L (b) as functions of thickness for the as-received and aged states. [Colour figure can be viewed at wileyonlinelibrary.com]

approximatively correspond. Above the critical thickness, both w_e and $J_{0.2}$ decrease and a plateau value is found for CT specimens (all geometries) at about 255 kJ/m^2. As in the case of the as-received material, no sharp drop in toughness is observed above B_c. The constant value for $J_{0.2}$ corresponds to the fact that all tests are valid.

The slope of $w_f - l_0$ curve corresponds to an energy dissipated per unit of volume (w_p) according to Equation (5). This equation can be rewritten as follows [19, 20, 27, 66]:

$$W_f = l_0 t_0 w_e + \beta l_0^2 t_0 \tilde{w}_p \quad \Rightarrow \quad w_f = w_e + l_0 \beta \tilde{w}_p = w_e + l_0 w_p \quad (8)$$

where β is a shape factor related to the form of the plastic dissipation zone. It can be taken as value of $\pi/4$ and $\pi h/4L$ for circular and elliptical zones, respectively [67], where L and h are the width and height of plastic zone. In this case, the slope is

$$\beta \tilde{w}_p = w_p \quad (9)$$

$\tilde{w}_p$ is the plastic work per unit of volume (i.e., the specific plastic work), which could be considered as constant. In [19, 21, 27, 68], which use Equation (8), a different slope is used for each investigated thickness, thus assuming that β varies with thickness. In this study, the shape of the plastic zone was analyzed using results from digital image correlation. The plastic zone is defined as the zone where the axial strain exceeds 3%. This value was found to allow for the definition of a well-defined separation between the elastic and plastic zones (see example in Figure 15b). The width (L) and height (h) of plastic zone are then measured using ImageJ [69]. Results are shown in Figure 15b for the load step corresponding to the maximum force. The scatter results from the test results of different ligament lengths. In the case of the as-received material, h/L slightly increases (1.5–1.6) with increasing thickness, whereas it decreases for the aged material (1.0–0.8). Using these values, $\tilde{w}_p$ was then determined using the experimentally determined value for w_p. This leads to an almost constant value for $\tilde{w}_p$ for both materials (56 N/mm^2 and 31 N/mm^2 for the as-received and aged materials respectively as shown in Figure 15a). Therefore, it appears to be better to fit one slope per thickness (i.e., taking Equation (8) into consideration) provided the shape of the plastic zone can be estimated. Note that w_p and h/L cannot be calculated from the elastoplastic simulations as damage must be accounted for.

7 | Conclusions

To study the size and thickness effect on fracture toughness, tensile tests, CT, and DENT tests are carried out with specimens of different geometries. The material studied is a 316 L(N) type stainless steel in an as-received state and an aged state (750°C during 2000 h).

1. Fractographic analysis of tensile and fracture toughness specimens shows a typical ductile fracture surface with large dimples at the as-received state. Particles are found in dimples, which are inclusions made of Al-Mg-O and CaS (core/shell structure). The damage mechanism is mainly inclusion cracking and interface decohesion. But in the aged state, a mix of intergranular and intragranular fracture is observed with many minidimples, which are formed by damage of precipitates that are formed during the aging treatment. These precipitates contribute to the reduction of the material ductility and to the increased of work hardening as it is observed on tensile properties.
2. In CT tests with specimens of different thicknesses, $J-R$ curves show a dependence of the blunting line on thickness, which is different from any standards. Therefore, $J_{0.2}$ values are determined by an adjusted blunting line. None of tests at as-received state is valid because $J_{0.2} > J_{max}$. There exists a nonmonotonic evolution of $J_{0.2}$ as a function of thickness. However, all tests at the aged state are valid ($J_{0.2} < J_{max}$). $J_{0.2}$ is stable but much smaller than for the as-received state. Thus, the aging process greatly reduces fracture toughness.
3. For tests with homothetic CT specimens, the same blunting line is found for the different sizes even when tests are not valid as in the as-received state. For valid tests in the aged state, no size effect is found, except in the case of the miniature specimens (CT8B4), which leads to a larger fracture toughness.
4. DENT tests show that the essential work w_e is an equivalent measure to $J_{0.2}$. It extends the nonmonotonic evolution of $J_{0.2}$ at small thicknesses.
5. For the determination of essential work w_e, slopes depending on the specimen thickness should be considered when fitting the linear relation between w_f and l_0. The specific plastic work $\tilde{w}_p$ appears to be a material constant independent of the specimen thickness. This requires the evaluation of the shape of the plastic zone.
6. The critical thickness for which the fracture toughness is maximum depends on the material, as shown by the simultaneous consideration of the results of the two types of fracture toughness tests. A larger ductility of the material results in an increased critical thickness.

Author Contributions

Sihan Cheng: conceptualization, data curation, formal analysis, methodology, software, investigation, writing – original draft. **Jérôme Garnier:** project administration, data curation, supervision, investigation, writing – review and editing. **Bernard Marini:** supervision, conceptualization, writing – review and editing. **Yazid Madi:** investigation, data curation, formal analysis, writing – review. **Jacques Besson:** supervision, methodology, conceptualization, writing – review and editing.

Acknowledgments

This work was fully funded and supported by the French Alternative Energies and Atomic Energy Commission, within the project R4G. The authors wish to thank Jean-Luc Flament, Aron N'Semi Noah, Amélie Gangloff, Elodie Rouesne, and Abdennour Meddour for their contribution to the mechanical tests and microscopic observations.

Conflicts of Interest

The authors declare no conflicts of interest.

Data Availability Statement

The data that support the findings of this study are available from the corresponding author upon reasonable request.

References

1. X. Li, C. Liu, X. Wang, et al., "Effect of Microstructure on Small Fatigue Crack Initiation and Early Propagation Behavior in Super Austenitic Stainless Steel 654SMO," *International Journal of Fatigue* 179 (2024): 108022.

2. K. Fang, K. Luo, and L. Wang, "Effect of Microstructure on Mechanical Properties of 316 LN Austenitic Stainless Steel," *Coatings* 12, no. 10 (2022): 1461.

3. Z. Chen, J. Pan, T. Jin, Z. Hong, and Y. Wu, "Estimation of Fracture Toughness of 16MnDR Steel Using Master Curve Method and Charpy V-Notch Impact Energy," *Theoretical and Applied Fracture Mechanics* 96 (2018): 443–451.

4. S. Zhang, S. Zhou, M. Li, and B. Fu, "Calculation and Comparison on Fracture Toughness of Specific Reliability Between ASTM and ISO Standards," *Materials Research Express* 7, no. 2 (2020): 026529.

5. A. Cheng, N. Z. Chen, and Y. Pu, "An Energy Principles Based Model for Fatigue Crack Growth Prediction," *International Journal of Fatigue* 128 (2019): 105198.

6. K. N. Pandey and S. Chand, "An Energy Based Fatigue Crack Growth Model," *International Journal of Fatigue* 25, no. 8 (2003): 771–778.

7. W. Brocks, P. Anuschewski, and D. Hellmann, "A Concept for Scaling J-R Curves by Plastic Constraint Factors," *International Journal of Fracture* 130, no. 1 (2004): 455–469.

8. J. R. Bloom, D. R. Lee, and W. V. D. Sluys, "An Investigation of Size and Constraint Effects on Ductile Crack Growth," in *Constraint Effects in Fracture* (ASTM International, 1993): 383–417.

9. Y. L. Kang, Z. F. Zhang, H. W. Wang, and Q. H. Qin, "Experimental Investigations of the Effect of Thickness on Fracture Toughness of Metallic Foils," *Materials Science and Engineering A* 394, no. 1 (2005): 312–319.

10. D. Frómeta, S. Parareda, A. Lara, et al., "Identification of Fracture Toughness Parameters to Understand the Fracture Resistance of Advanced High Strength Sheet Steels," *Engineering Fracture Mechanics* 229 (2020): 106949.

11. ASTM International, "ASTM E1820-23B: Standard Test Method for Measurement of Fracture Toughness," in *Annual Book of ASTM Standards* (ASTM International, 2023).

12. ISO, "ISO 12135: Unified Method of Test for the Determination of Quasistatic Fracture Toughness," International Organization for Standardization, (2021).

13. H. Ono, R. Kasada, and A. Kimura, "Specimen Size Effects on Fracture Toughness of JLF-1 Reduced-Activation Ferritic Steel," *Journal of Nuclear Materials* 329 (2004): 1117–1121.

14. ASTM International, "ASTM E1820-99A: Standard Test Method for Measurement of Fracture Toughness," in *Annual Book of ASTM Standards* (ASTM International, 1999).

15. S. Mahmoud and K. Lease, "The Effect of Specimen Thickness on the Experimental Characterization of Critical Crack-Tip-Opening Angle in 2024-T351 Aluminum Alloy," *Engineering Fracture Mechanics* 70, no. 3 (2003): 443–456.

16. A. R. Shahani, M. Rastegar, M. Botshekanan Dehkordi, and K. H. Moayeri, "Experimental and Numerical Investigation of Thickness Effect on Ductile Fracture Toughness of Steel Alloy Sheets," *Engineering Fracture Mechanics* 77, no. 4 (2010): 646–659.

17. M. F. Kanninen and C. A. Popelar, *Advanced Fracture Mechanics* (Oxford University Press, 1985).

18. C. S. Seok and S. Y. Kim, "Effect of Specimen Configurations on the Fracture Resistance Curve," *Nuclear Engineering and Design* 214, no. 1 (2002): 47–56.

19. T. Pardoen, Y. Marchal, and F. Delannay, "Thickness Dependence of Cracking Resistance in Thin Aluminium Plates," *Journal of the Mechanics and Physics of Solids* 47, no. 10 (1999): 2093–2123.

20. T. Pardoen, Y. Marchal, and F. Delannay, "Essential Work of Fracture Compared to Fracture Mechanics-Towards a Thickness Independent Plane Stress Toughness," *Engineering Fracture Mechanics* 69, no. 5 (2002): 617–631.

21. S. Sahoo, N. Padmapriya, P. S. De, P. C. Chakraborti, and S. K. Ray, "Ductile Tearing Resistance Indexing of Automotive Grade DP 590 Steel Sheets: EWF Testing Using DENT Specimens," *Journal of Materials Engineering and Performance* 27, no. 4 (2018): 2018–2023.

22. Y. Marchal, J. F. Walhin, and F. Delannay, "Statistical Procedure for Improving the Precision of the Measurement of the Essential Work of Fracture of Thin Sheets," *International Journal of Fracture* 87, no. 2 (1997): 189–199.

23. B. Cotterell and J. K. Reddel, "The Essential Work of Plane Stress Ductile Fracture," *International Journal of Fracture* 13, no. 3 (1977): 267–277.

24. Y. W. Mai and K. M. Pilko, "The Essential Work of Plane Stress Ductile Fracture of a Strain-Aged Steel," *Journal of Materials Science* 14, no. 2 (1979 Feb): 386–394.

25. B. Cotterell, T. Pardoen, and A. G. Atkins, "Measuring Toughness and the Cohesive Stress–Displacement Relationship by the Essential Work of Fracture Concept," *Engineering Fracture Mechanics* 72, no. 6 (2005): 827–848.

26. J. Pujante, D. Frómeta, E. Garcia-Llamas, M. Gimenez, and D. Casellas, "Hot Stamped Aluminium for Crash-Resistant Automobile Safety Cage Applications," *Materials Science Forum* 1016 (2021): 445–452.

27. T. Bárány, T. Czigány, and J. Karger-Kocsis, "Application of the Essential Work of Fracture (EWF) Concept for Polymers, Related Blends and Composites: A Review," *Progress in Polymer Science* 35, no. 10 (2010): 1257–1287.

28. J. Wu and Y. W. Mai, "The Essential Fracture Work Concept for Toughness Measurement of Ductile Polymers," *Polymer Engineering and Science* 36, no. 18 (1996): 2275–2288.

29. E. Lucon and M. Scibetta, "Miniature Compact Tension Specimens for Upper Shelf Fracture Toughness Measurements on RPV Steels," in *Small Specimen Test Techniques: 5th Volume*, vol. 5 (ASTM International, 2008): 1–10.

30. G. Wardle, "A Study of Specimen Size Effects on the Initiation Toughness and Tearing Resistance of an A533B-1 Steel," in *Small Specimen Test Techniques: Fourth Volume* (ASTM International, 2022): 48–66.

31. J. K. L. Lai, "A Study of Precipitation in AISI Type 316 Stainless Steel," *Materials Science and Engineering* 58, no. 2 (1983): 195–209.

32. C. Ma, Q. Peng, J. Mei, E. H. Han, and W. Ke, "Microstructure and Corrosion Behavior of the Heat Affected Zone of a Stainless Steel 308L-316L Weld Joint," *Journal of Materials Science and Technology* 34, no. 10 (2018): 1823–1834.

33. V. Vodárek, "Creep Behaviour and Microstructural Evolution in AISI 316LN+Nb Steels at 650°C," *Materials Science and Engineering A* 528, no. 12 (2011): 4232–4238.

34. A. F. Padilha and P. R. Rios, "Decomposition of Austenite in Austenitic Stainless Steels," *ISIJ International* 42, no. 4 (2002): 325–327.

35. S. Zheng, C. Li, Y. Qi, L. Chen, and C. Chen, "Mechanism of (Mg,Al,Ca)-Oxide Inclusion-Induced Pitting Corrosion in 316L Stainless Steel Exposed to Sulphur Environments Containing Chloride Ion," *Corrosion Science* 67 (2013): 20–31.

36. X. Yin, Y. H. Sun, Y. D. Yang, et al., "Inclusion Evolution During Refining and Continuous Casting of 316L Stainless Steel," *Ironmaking and Steelmaking* 43, no. 7 (2016): 533–540.

37. C. Y. Jeong, K. J. Kim, H. U. Hong, and S. W. Nam, "Effects of Aging Temperature and Grain Size on the Formation of Serrated Grain Boundaries in an AISI 316 Stainless Steel," *Materials Chemistry and Physics* 139, no. 1 (2013): 27–33.

38. D. N. Githinji, S. M. Northover, P. J. Bouchard, and M. A. Rist, "An EBSD Study of the Deformation of Service-Aged 316 Austenitic Steel," *Metallurgical and Materials Transactions a.* 44, no. 9 (2013): 4150–4167.

39. M Rieth, A Falkenstein, P Graf, et al., "Creep of the Austenitic Steel AISI 316L (N)," Experiments and Models, (2004).

40. K. Kimura, M. Murata, K. Kamihira and H Tanaka, "Creep Strength and Microstructural Evolution of Type 316L(N) Stainless Steel" Proc ECCC Creep & Fracture. (2014); 5–7.

41. F. Stein and A. Leineweber, "Laves Phases: A Review of Their Functional and Structural Applications and an Improved Fundamental Understanding of Stability and Properties," *Journal of Materials Science* 56, no. 9 (2021): 5321–5427.

42. V. Vilamosa, A. H. Clausen, E. Fagerholt, O. S. Hopperstad, and T. Børvik, "Local Measurement of Stress–Strain Behaviour of Ductile Materials at Elevated Temperatures in a Split-Hopkinson Tension bar System," *Strain* 50, no. 3 (2014): 223–235.

43. C. Defaisse, M. Mazière, L. Marcin, and J. Besson, "Ductile Fracture of an Ultra-High Strength Steel Under Low to Moderate Stress Triaxiality," *Engineering Fracture Mechanics* 194 (2018): 301–318.

44. S. Tu, X. Ren, T. A. Kristensen, J. He, and Z. Zhang, "Study of Low-Temperature Effect on the Fracture Locus of a 420-MPa Structural Steel With the Edge Tracing Method," *Fatigue and Fracture of Engineering Materials and Structures* 41, no. 8 (2018): 1649–1661.

45. Z. Shokeir, J. Besson, C. Belhadj, T. Petit, and Y. Madi, "Edge Tracing Technique to Study Post-Necking Behavior and Failure in Al Alloys and Anisotropic Plasticity in Line Pipe Steels," *Fatigue and Fracture of Engineering Materials and Structures* 45, no. 9 (2022): 2427–2442.

46. X. Xu, S. Xu, L. Jin, and E. Song, "Characteristic Analysis of Otsu Threshold and Its Applications," *Pattern Recognition Letters* 32, no. 7 (2011): 956–961.

47. A. A. Abduluyahed and K. J. Kurzydłowski, "Tensile Properties of a Type 316 Stainless Steel Strained in Air and Vacuum," *Materials Science and Engineering A* 256, no. 1 (1998): 34–38.

48. S. Y. Chen and D. Gan, "Effects of Grain Boundary Carbides on the Tensile and Impact Properties of Type 316 Stainless Steel," *Materials Science and Engineering* 84 (1986): 65–76.

49. D. Fahr "Analysis of Stress-Strain Behavior of Type 316 Stainless Steel," In: Technical Report: ORNL-TM-4292. US: Oak Ridge National Laboratory; (1973).

50. E. Voce, "The Relationship Between Stress and Strain for Homogeneous Deformation," *Journal of the Institute of Metals* 74 (1948): 537–562.

51. J. R. Rice, P. C. Paris, and J. G. Merkle, "Some Further Results of J-Integral Analysis and Estimates," in *Progress in Flaw Growth and Fracture Toughness Testing*, eds. J. G. Kaufman, J. L. Swedlow, H. T. Corten, J. E. Srawley, R. H. Heyer, et al. (ASTM International, 1973): 231–245.

52. T. L. Anderson, *Fracture Mechanics: Fundamentals and Applications* (CRC Press, 2005).

53. A. Nishimura, N. Inoue, and T. Muroga, "Fracture Toughness of Low Activation Ferritic Steel (JLF-1) Weld Joint at Room Temperature," *Journal of Nuclear Materials* 258 (1998): 1242–1247.

54. S. Mr, E. Schmidova, P. Konopík, et al., "Fracture Toughness Analysis of Automotive-Grade Dual-Phase Steel Using Essential Work of Fracture (EWF) Method," *Meta* 10, no. 8 (2020): 1019.

55. T. Petit, C. Ritter, J. Besson, and T. F. Morgeneyer, "Impact of Machine Stiffness on '"Pop-In"' Crack Propagation Instabilities," *Engineering Fracture Mechanics* 202 (2018): 405–422.

56. T. Pardoen, F. Hachez, B. Marchioni, P. H. Blyth, and A. G. Atkins, "Mode I Fracture of Sheet Metal," *Journal of the Mechanics and Physics of Solids* 52 (2004): 423–452.

57. S. Mr, E. Schmidova, P. Konopík, and D. Melzer, "Fracture Toughness Examination of Dual-Phase and Interstitial Free Steel Using Essential Work of Fracture Method," *Fatigue and Fracture of Engineering Materials and Structures* 44, no. 12 (2021): 3272–3288.

58. Y. Guo, T. L. Burnett, S. A. McDonald, M. Daly, A. H. Sherry, and P. J. Withers, "4D Imaging of Void Nucleation, Growth, and Coalescence From Large and Small Inclusions in Steel Under Tensile Deformation," *Journal of Materials Science and Technology* 123 (2022): 168–176.

59. H. Ding, T. Zhu, X. Wang, B. Yang, S. Xiao, and G. Yang, "An Uncoupled Ductile Fracture Model Considering Void Shape Change and Necking Coalescence," *Engineering Fracture Mechanics* 292 (2023): 109612.

60. D. Gan, "Tensile and Fracture Properties of Type 316 Stainless Steel After Creep," *Metallurgical Transactions a.* 13, no. 12 (1982): 2155–2163.

61. V. Ganesan, K. Laha, and M. D. Mathew, "Influence of Nitrogen Content on the Evolution of Creep Damage in 316 LN Stainless Steel," *Procedia Engineering* 86 (2014): 58–65.

62. X. Wang, C. Liu, Z. Zhou, Y. Zhang, and M. Huang, "In-Situ EBSD Investigation of Plastic Damage in a 316 Austenitic Stainless Steel and Its Molecular Dynamics (MD) Simulations," *Journal of Materials Research and Technology* 13 (2021): 823–833.

63. P. R. Sreenivasan, S. K. Ray, S. Vaidyanathan, and P. Rodriguez, "Measurement of Stretch Zone Height and Its Relationship to Crack tip Opening Displacement and Initiation J-Value in an AISI 316 Stainless Steel," *Fatigue and Fracture of Engineering Materials and Structures* 19 (1996): 855–868.

64. ASTM International, "ASTM E1820-08A: Standard Test Method for Measurement of Fracture Toughness," in *Annual Book of ASTM Standards* (ASTM International, 2008).

65. ASTM International, "ASTM E1820-11: Standard Test Method for Measurement of Fracture Toughness," in *Annual Book of ASTM Standards* (ASTM International, 2011).

66. M. Rink, L. Andena, and C. Marano, "The Essential Work of Fracture in Relation to J-Integral," *Engineering Fracture Mechanics* 127 (2014): 46–55.

67. Y. W. Mai, S. C. Wong, and X. H. Chen, "Application of Fracture Mechanics for Characterization of Toughness of Polymer Blends," *Polymer Blends: Formulations and Performance.* 2 (2000): 17–58.

68. J. Gamez-Perez, O. Santana, A. B. Martinez, and M. L. Maspoch, "Use of Extensometers on Essential Work of Fracture (EWF) Tests," *Polymer Testing* 27, no. 4 (2008): 491–497.

69. T Ferreira, W Rasband, "ImageJ User Guide," (2012).

70. "Commissariat à L'énergie Atomique et Aux Énergies Alternatives," Cast3M User Manual, (2023).

Appendix

The meshes used in simulations are shown below. Linear elements with full integration are used. The F-bar method is used to avoid pressure oscillations. The minimum mesh size is set to 0.2 mm. All simulations were carried out with the software Cast3M in the frame of the large deformation theory [70].

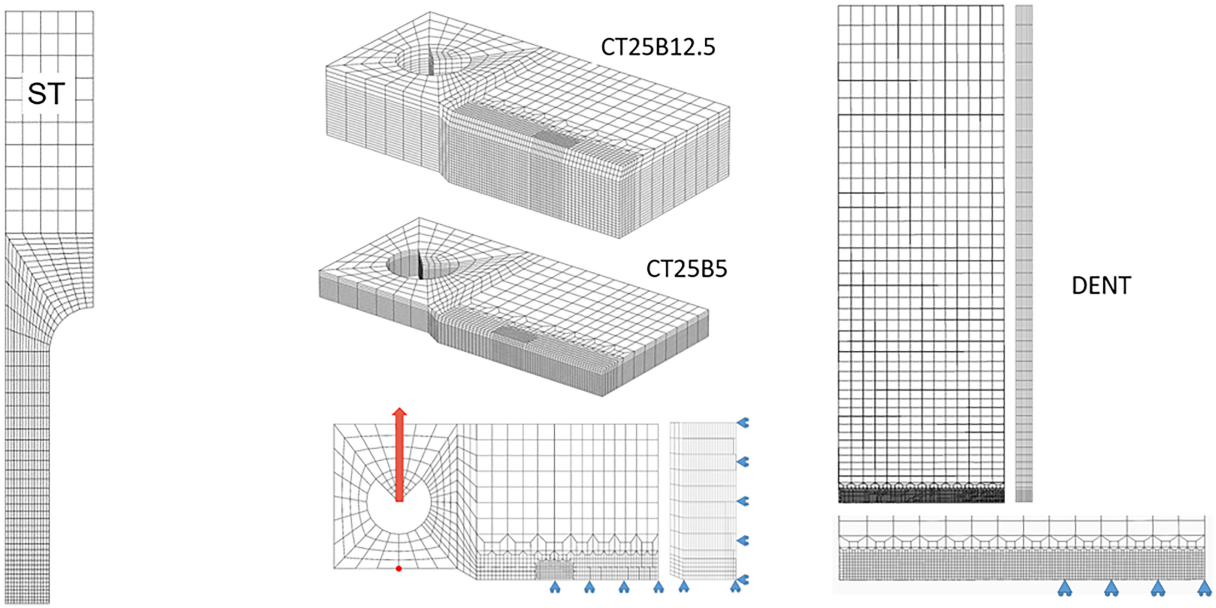

FIGURE A1 Finite element meshes used for the simulations.